

THE SNR PUPPIS A REVISITED WITH SEVEN YEARS OF FERMI LARGE AREA TELESCOPE OBSERVATIONS

YU-LIANG XIN^{1,2}, XIAO-LEI GUO^{1,3}, NENG-HUI LIAO^{1,4}, QIANG YUAN^{1,4}, SI-MING LIU^{1,4}, DA-MING WEI^{1,4}

Draft version September 11, 2018

ABSTRACT

Puppis A is a very famous and extensively studied supernova remnant (SNR) that shows strong evidence of shock-cloud interaction. We re-analyze the GeV γ -ray emission of it using seven years Pass 8 data recorded by the Fermi Large Area Telescope (Fermi-LAT). The morphology of the γ -ray emission is more compatible with that of the thermal X-ray and IR emissions than the radio image, which suggests a possible correlation between the gamma-ray emitting region and dense clouds. The γ -ray spectrum in the energy range of 1-500 GeV shows a break at 7.92 ± 1.91 GeV with the photon indices of 1.81 ± 0.08 below the break and 2.53 ± 0.12 above the break, which can naturally explain the lack of TeV γ -ray emission from Puppis A. The multi-wavelength observations favor a hadronic origin for the γ -ray emission.

Subject headings: ISM: supernova remnants—Gamma rays: general—Radiation mechanisms: non-thermal

1. INTRODUCTION

Supernova remnants (SNRs) are widely believed to be the most probable acceleration sites of Galactic cosmic rays (CRs) below energies of the knee (see Hillas 2005, for a review). The high energy γ -ray emission can pinpoint the presence of energetic electrons or nuclei. SNRs interacting with dense molecular clouds (MCs) are expected to be a class of the brightest sources in the γ -ray band. Indeed, the γ -ray emission from several sources of this class has been detected by the Fermi Large Area Telescope (Fermi-LAT), including IC443 (Abdo et al. 2010a; Ackermann et al. 2013), W44 (Abdo et al. 2010b; Ackermann et al. 2013), W28 (Abdo et al. 2010c; Hanabata et al. 2014), W51C (Abdo et al. 2009), W49B (Abdo et al. 2010d), W30 (Ajello et al. 2012), Tycho (Zhang et al. 2013), Kesteven 27 (Xing et al. 2015), and Kesteven 41 (Liu et al. 2015). The intense GeV γ -ray emission from these SNRs is generally believed to be from the decay of neutral pions produced in inelastic collisions between accelerated protons and the dense gas in MCs. Especially, γ -ray spectra of IC443, W44 and W51C have shown spectral feature of π^0 decay⁵ (Giuliani et al. 2011; Ackermann et al. 2013; Jogler & Funk 2016), which are considered the most direct evidence for the presence of relativistic nuclei acceleration in SNRs.

In addition, the γ -ray spectra of most SNRs mentioned above exhibit remarkable spectral breaks in the 1-20 GeV band, steepening above the break energy. The spectral break can be explained by the energy-dependent diffusion of accelerated particles from the SNR shell into nearby molec-

ular clouds (Aharonian & Atoyan 1996; Gabici et al. 2009; Ohira et al. 2011; Li & Chen 2010, 2012), the re-acceleration in crushed clouds (Uchiyama et al. 2010) or the Alfvén wave evanescence in weakly ionized dense gas (Malkov et al. 2011).

Puppis A (G260.4-3.4) is a famous SNR with evident interaction with MCs. Its distance was determined to be 2.2 ± 0.3 kpc based on the observation of neutral hydrogen (Reynoso et al. 2003). At such a distance the diameter of Puppis A is estimated to be about 30 pc. A central compact object (CCO), RX J0822-4300, is located near the geometric center of Puppis A, which has been identified as the stellar remnant left after the supernova (SN) explosion (Petre et al. 1996; Zavlin et al. 1999). Based on observations of the proper motion of the CCO and optical filaments, the age of Puppis A was estimated to be (4450 ± 750) yr (Becker et al. 2012; Winkler et al. 1988), implying that this SNR is in the Sedov-Taylor evolutionary phase. There are two bright knots inside Puppis A, including the “bright eastern knot” and the “bright northern knot” (Petre et al. 1982). The X-ray spectral studies revealed correlation between these knots and the shock-cloud interaction, making Puppis A to be the first X-ray-identified example of shock-cloud interaction in a relatively late phase of evolution (Hwang et al. 2005; Katsuda et al. 2010, 2012). No dense molecular gas is adjacent to the eastern knot, implying that the molecular clumps have been completely engulfed and destroyed by the shock front (Paron et al. 2008). The shock velocity of Puppis A is $\sim (600-1200)$ km s⁻¹, which was derived according to the oxygen and electron temperatures as well as the ionization timescale in the ejecta knot (Katsuda et al. 2013).

Puppis A is one of the brightest SNRs in the X-ray band. Each area of it has been observed by several X-ray telescopes in orbit, e.g., *Einstein* (Petre et al. 1982), *ROSAT* (Aschenbach et al. 1993), *Suzaku* (Hwang et al. 2008), *Chandra* (Hwang et al. 2005; Dubner et al. 2013), and *XMM-Newton* (Hui & Becker 2006; Katsuda et al. 2010, 2012; Dubner et al. 2013). The X-ray emission detected is completely thermal in origin, which mostly comes from the shocked interstellar medium (ISM; Hwang et al. 2005) except that there are a few isolated O-Ne-Mg-rich features associated with the SN ejecta (Hwang et al. 2005; Katsuda et al. 2008, 2010, 2013). Recently, Dubner et al.

E-mail: yuanq@pmo.ac.cn (QY); liusm@pmo.ac.cn (SML); dmwei@pmo.ac.cn (DMW)

¹ Key laboratory of Dark Matter and Space Astronomy, Purple Mountain Observatory, Chinese Academy of Sciences, Nanjing 210008, China;

² University of Chinese Academy of Sciences, Yuquan Road 19, Beijing, 100049, China;

³ Department of Physics and Institute of Theoretical Physics, Nanjing Normal University, Nanjing 210046, China

⁴ School of Astronomy and Space Science, University of Science and Technology of China, Hefei, Anhui 230026, China

⁵ Note that the peak of the π^0 decay spectrum is at half the π^0 mass, 67.5 MeV, so is not properly covered by present experiments to date. Hence the π^0 signature is of limited significance up to now, but should be addressable with future Fermi-LAT data or future experiments such as e-ASTROGAM (Tatischeff et al. 2016) which extend to lower energies as required to detect the peak.

(2013) showed the most complete and detailed X-ray view of Puppis A and confirmed that the SNR evolves in an inhomogeneous, probably knotty ISM. The hard component of the X-ray emission is spatially coincident with the distribution of neutral hydrogen column densities, implying the absorption of soft photons by neutral hydrogens (Dubner et al. 2013; Reynoso et al. 2003). The infrared (IR) images, observed by the *Spitzer* Space Telescope, revealed an extremely good correlation with the X-ray emission, demonstrating that the thermal IR emission arises from swept-up interstellar dust, collisionally heated by the hot shocked gas (Arendt et al. 2010).

Hewitt et al. (2012) reported the detection of GeV γ -ray emission from Puppis A with the Fermi-LAT. With a luminosity of only $2.7 \times 10^{34} (d/2.2 \text{ kpc})^2 \text{ erg s}^{-1}$ between 1 and 100 GeV, Puppis A is among the faintest SNRs identified by the Fermi-LAT. The morphology of the GeV γ -ray emission is spatially extended, which is compatible with the X-ray morphology. The γ -ray emission is well described by a power law spectrum with an index of 2.1. Considering the multi-wavelength data from the radio to γ -ray, both leptonic and hadronic models are possible with different magnetic field strengths and different energies of relativistic particles. In addition, Hewitt et al. (2012) also reported a hint of a radio break or cutoff at ~ 40 GHz using 7 years data from the *Wilkinson Microwave Anisotropy Probe* (WMAP).

Abramowski et al. (2015) observed Puppis A in the very-high-energy (VHE; $E \geq 0.1$ TeV) band with the High Energy Stereoscopic System (HESS). However, no significant VHE emission has been detected. It has been suggested that the lack of the VHE signal implies that a spectral break or cutoff would occur at 280 or 450 GeV, assuming a power law with a simple exponential or a sub-exponential cutoff, respectively (Abramowski et al. 2015).

In this work, we report the detection of the GeV break in the spectrum of Puppis A, with the Pass 8 data recorded by the Fermi-LAT. In Section 2, the data analysis and results are presented, including the spatial and spectral analyses. The discussion about the origin of the non-thermal emission based on the multi-wavelength data is given in Section 3, followed by conclusions in Section 4.

2. DATA ANALYSIS

2.1. Data reduction

We analysis the SNR Puppis A using the latest Pass 8 version of the Fermi-LAT data taken in the period between August 4, 2008 (Mission Elapsed Time 239557418) to August 4, 2015 (Mission Elapsed Time 460339204). The Galactic coordinate of Puppis A is (260.4, -3.4). It is close to the Galactic plane, but in a direction of the outer Galaxy. The surface brightness of the Galactic diffuse emission is smaller by a factor of ~ 2 than that of Puppis A. A very bright gamma-ray source, the Vela pulsar, is about 3 degrees away from Puppis A, which actually affects the low energy analysis of Puppis A. Therefore, to prevent event contamination from the nearby Vela pulsar, only events with energies above 1 GeV are selected. We select the “source” event class (ev-class=128 & evttype=3) and exclude the data with zenith angle greater than 90° to minimize contamination from the Earth limb. This analysis is performed within a square region of $14^\circ \times 14^\circ$ centered at the position of Puppis A (R.A.= 125.66°, Dec.= -42.84° ; Acero et al. 2015), which is referred to as a region of interest (ROI). We use the standard LAT analy-

sis software, *ScienceTools* version v10r0p5⁶, available from the Fermi Science Support Center, and adopt the instrumental response function (IRF) “P8R2_SOURCE_V6”. The binned likelihood analysis method with *gtlike* is used to fit the data. For the background subtraction, the diffuse backgrounds including the Galactic emission and the isotropic component, are modeled according to *gll_iem_v06.fits* and *iso_P8R2_SOURCE_V6_v06.txt*⁷. All sources in the third Fermi catalog (3FGL; Acero et al. 2015) within a radius of 15° from the ROI center are included in the source model, which is generated with the user-contributed software *make3FGLxml.py*⁸. Except that, two extra point sources, named as source A (R.A.= 129.707°, Dec.= -44.083°) and source B (R.A.= 122.273°, Dec.= -47.293°), which are not in the 3FGL catalog are added to the model. During the fitting analysis, the normalizations and spectral parameters of all sources within a distance of 7° from the ROI center, together with the normalizations of the two diffuse backgrounds, are left free.

2.2. Spatial correlations

The gamma-ray emission from Puppis A is extended. And an uniform disk with a radius of 0.37° is suggested by the Fermi-LAT collaboration as the spatial template for Puppis A (Acero et al. 2015). In order to show the spatial correlation between the γ -ray and other energy bands, we created two residual counts maps by subtracting the best-fit model maps from the counts maps for photons above 5 GeV (top) and 10 GeV (bottom) in Fig. 1 using the PSF3-type data (ev-class=128 & evttype=32), which has the best spatial resolution. The radio contours at 843 MHz from the Sydney University Molonglo Sky Survey (SUMSS; Mauch et al. 2003), the X-ray contours from *ROSAT* High Resolution Imager (HRI; Petre et al. 1996) and the infrared (IR) contours from IRAS satellite (Miville-Deschênes & Lagache 2005) are overplotted. The residual maps reveal that the GeV emission of Puppis A mainly concentrates in the northeast (NE) region and extends into the southwest (SW) region, which is more compatible with the X-ray/IR than the radio morphology.

Besides the uniform disk template, we also used three additional spatial templates according to multi-wavelength observations to fitting the γ -ray emission of Puppis A: the radio image at 843 MHz from SUMSS (Mauch et al. 2003), the X-ray image from *ROSAT* HRI (Petre et al. 1996), and the infrared (IR) image from IRAS satellite (Miville-Deschênes & Lagache 2005). The photon flux and TS value for each spatial template are list in Table 1. As can be seen, the TS value for the X-ray image is larger than that for the uniform disk, even though the spatial template of an uniform disk has more degrees of freedom. Comparing with the radio image, the X-ray/IR one is more consistent with the morphology of the γ -ray emission for the relatively higher TS value.

Hereafter, we adopt the X-ray image with the highest TS value as the spatial template for the whole SNR in the following spectral analysis.

2.3. Spectral analysis

We perform a spectral analysis of Puppis A in the energy range from 1 GeV to 500 GeV with the spatial tem-

⁶ <http://fermi.gsfc.nasa.gov/ssc/data/analysis/software/>

⁷ <http://fermi.gsfc.nasa.gov/ssc/data/access/lat/BackgroundModels.html>

⁸ <http://fermi.gsfc.nasa.gov/ssc/data/analysis/user/>

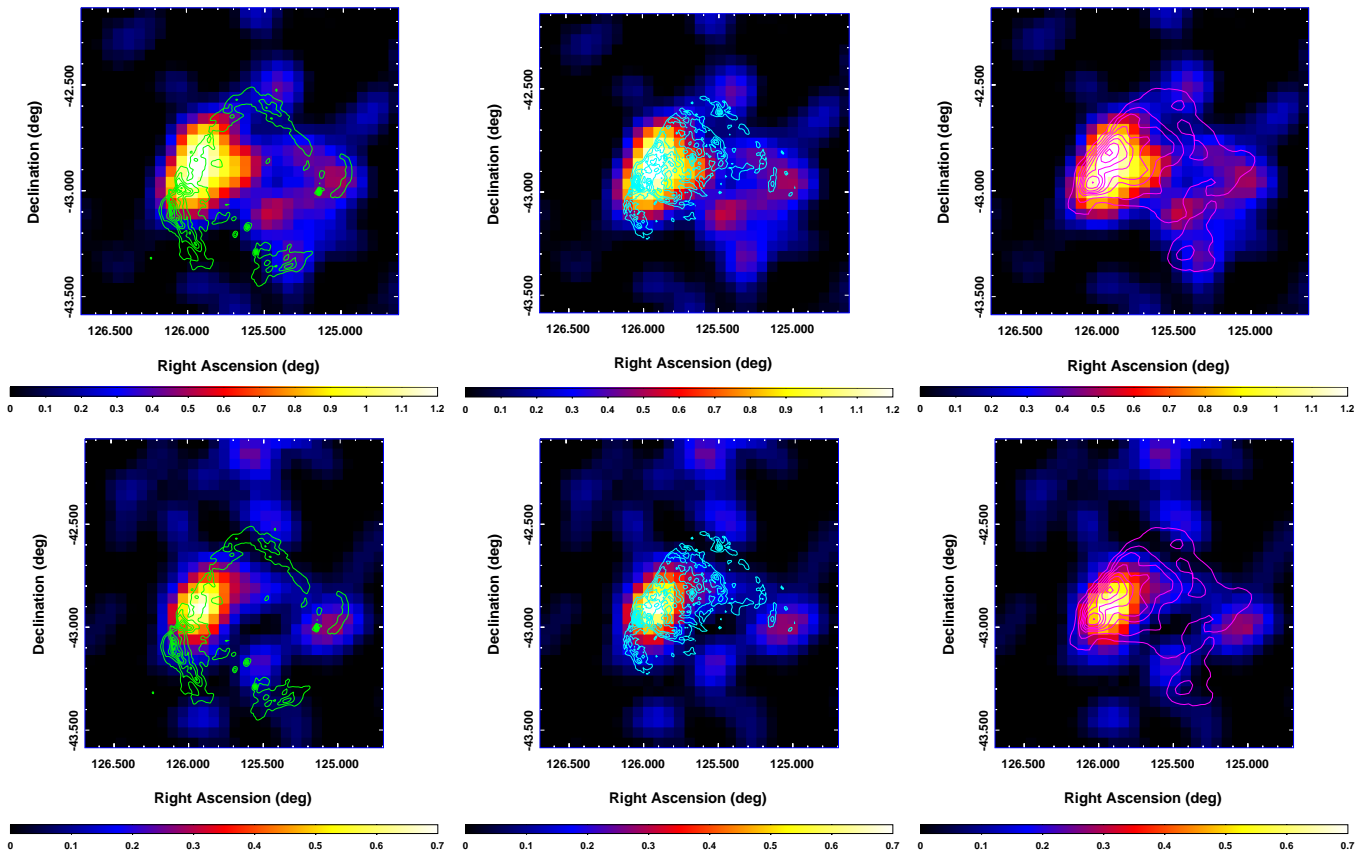


FIG. 1.— Residual counts maps of $1.5^\circ \times 1.5^\circ$ region centered at Puppis A for photons above 5 GeV (PSF3-type data; top images) and 10 GeV (PSF3-type data; bottom images), derived by subtracting the best-fit model maps from the counts maps. These maps are smoothed with a Gaussian kernel of $\sigma = 0.2^\circ$. Green contours (left) represent the radio image of Puppis A at 843 MHz from SUMSS (Mauch et al. 2003); cyan contours (middle) show the *ROSAT* HIR image of X-ray emission (Petre et al. 1996) and magenta contours (right) display the IR image from IRAS satellite (Miville-Deschênes & Lagache 2005).

TABLE 1
SPATIAL DISTRIBUTION ANALYSIS FOR PUPPIS A BETWEEN 1 GEV AND 500 GEV

Spatial Template	Photon Flux (10^{-9} ph cm^{-2} s^{-1})	TS value	Degrees of Freedom
Uniform disk	8.23 ± 0.29	1825.9	5
X-ray image	8.31 ± 0.29	1890.4	2
Radio image	8.28 ± 0.30	1527.6	2
Infrared image	9.47 ± 0.33	1650.3	2

plate of the X-ray image using the binned likelihood analysis method. First, we adopt a simple power law (PL) spectrum to fit the data. The spectral index is found to be 2.07 ± 0.03 , and the integral photon flux is $(8.31 \pm 0.29) \times 10^{-9}$ photon cm^{-2} s^{-1} , which is in agreement with the results given by Hewitt et al. (2012). We then test for a break in the spectrum of Puppis A using a broken power law (BPL) spectrum. Significant improvement of the fitting can be found compared with the single PL model. The results from the spectral fits are summarized in Table 2. We tested for the significance of this spectral break using a likelihood ratio test: $\text{TS}_{\text{break}} = -2 \ln(L_{\text{PL}}/L_{\text{BPL}})$, where L_{PL} and L_{BPL} represent the likelihoods for the simple PL model and BPL model, respec-

tively. We obtain $\text{TS}_{\text{break}} = 35.4$, which corresponds to a significance of $\sim 5.6\sigma$ for two additional degrees of freedom. Thus we conclude that the spectrum of Puppis A does have a break at 7.92 ± 1.91 GeV. The existence of the break and a relatively soft spectrum above the break energy, $\gamma_2 = 2.53$, can naturally explain the non-detection in the VHE γ -ray band (Abramowski et al. 2015).

Furthermore, to derive the γ -ray spectrum of Puppis A, we bin the data with 15 logarithmically even energy bins between 1 GeV and 500 GeV, and perform the same likelihood fitting analysis to the data and the results are listed in Table 3. The obtained energy spectrum weighted by E^2 , overplotted with the best-fit BPL result, is shown in the top panel of Fig. 2. Note that the break of the spectrum should not be confused with the so-called π^0 peak of the photon spectrum, whose energy is much lower than that covered by our analysis (see the bottom panel of Fig. 2 for an explicit illustration).

We also search for spectral difference between the eastern and the western regions of Puppis A, with a half-disk template each. The spectral data points of the eastern and the western regions are listed in Table 3. The spectra are shown in the top and the bottom panels of Fig. 3, with the best-fitting spectra of each region overplotted. We find that the spectrum of the eastern region also shows a break with $E_b \sim 3$ GeV, while for the

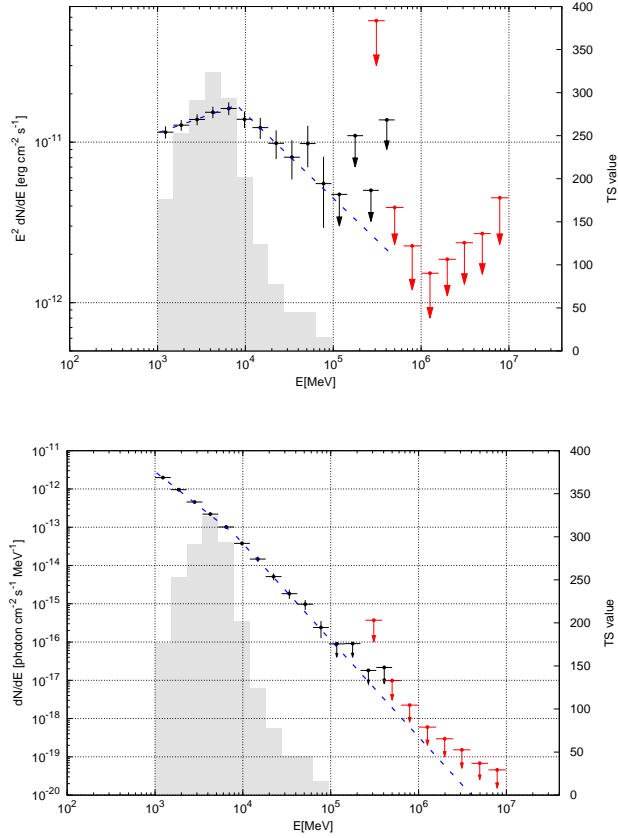


FIG. 2.— The E^2 weighted energy spectrum (top) and photon spectrum (bottom) of the total SNR. The results of Fermi-LAT data are shown by black dots, with arrows indicating the 95% upper limits. The gray histogram denotes the TS value for each energy bin. The upper limits in the TeV band (red) are from HESS observations (Abramowski et al. 2015). The best-fit BPL spectrum in the energy range from 1 GeV to 500 GeV is overlotted with the blue dashed line.

western region a single PL is able to describe the GeV emission. However, considering the upper limit in the TeV band, a break or cutoff should be needed for the western region.

TABLE 2

SPECTRAL FIT PARAMETERS FOR PL AND BPL BETWEEN 1 GeV AND 500 GeV WITH THE SPATIAL TEMPLATE OF THE X-RAY IMAGE

Spectral model	γ_1	γ_2	E_b (GeV)	Photon Flux (10^{-9} ph cm $^{-2}$ s $^{-1}$)	TS value
PL	2.07 ± 0.03	—	—	8.31 ± 0.29	1890.4
BPL	1.81 ± 0.08	2.53 ± 0.12	7.92 ± 1.91	8.01 ± 0.29	1925.8

3. DISCUSSION

3.1. Morphology and γ -ray spectrum

From the above analysis, the GeV γ -ray emission is spatially well correlated with the morphology in the X-ray/IR rather than the radio band, which means that there should be some dense clouds in the γ -ray emitting region (Dubner et al. 2013; Abramowski et al. 2015). However, no CO emission was detected in such regions, which can be attributed to dissociation of molecules by the radiative precursor of the SNR due to the photoionization and photodissociation effects (Paron et al. 2008) or there is some CO-dark gas in the γ -ray emitting region which can not be traced by CO observations

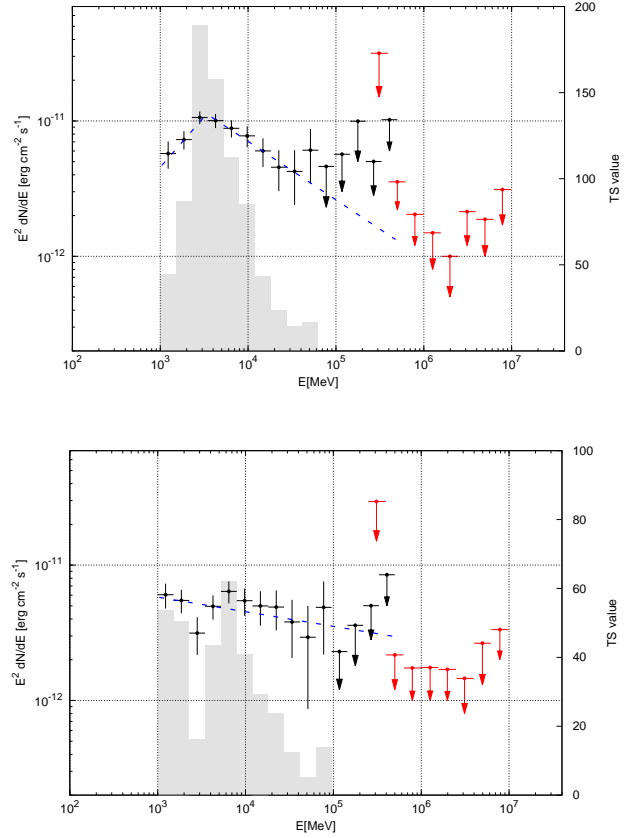


FIG. 3.— Same as the top panel of Fig. 2, but for the eastern (top) and western (bottom) regions of the SNR separately. For the western region, a single PL spectrum is adopted to fit the Fermi-LAT data.

(Grenier et al. 2005).

There may be another explanation for the spatial correspondence between the γ -ray and the X-ray emissions. Dubner et al. (2013) shows that Puppis A displays a softening of the X-ray emission from NE to SW region, corresponding to the variation of column density of neutral hydrogen (Reynoso et al. 2003; Hwang et al. 2005). The higher-density column in the NE region may be responsible for the absorption of soft X-ray photons resulting in the spatial distribution of the X-ray emission. Therefore, there may exist some dense HI clouds in the vicinity of the central part of Puppis A. These HI clouds are illuminated by energetic particles from Puppis A to emit strong γ -ray emissions.

Spatial correlation among the γ -ray and the thermal X-ray emission also exists in SNR W51C (Abdo et al. 2009) and Cygnus Loop (Katagiri et al. 2011). However, for W51C, the γ -ray emission is also consistent with the radio extension. And for Cygnus Loop, the morphology of the X-ray emission is shell-like and the H α filaments together with the radio continuum emission in the northern part of Cygnus Loop are correlated with the γ -ray emission spatially, which are very different from Puppis A. Humensky et al. (2015) reported that the γ -ray emission of the SNR IC443 is anticorrelated with its thermal X-ray emission, which is opposite to that of Puppis A.

The spectral analysis of Puppis A reveals the existence of a break at 7.92 ± 1.91 GeV in the spectrum and the GeV break is usually linked to SNRs interacting with molecular clouds, like IC443, W44 and W51C, etc. These SNR/MC

TABLE 3
FERMI-LAT SPECTRAL DATA POINTS OF PUPPIS A

Energy band (GeV)	photon flux of total SNR (ph cm ⁻² s ⁻¹)	TS value of total SNR	photon flux of eastern region (ph cm ⁻² s ⁻¹)	TS value of eastern region	photon flux of western region (ph cm ⁻² s ⁻¹)	TS value of western region
1.00 – 1.51	$(2.44 \pm 0.21) \times 10^{-9}$	175.6	$(1.22 \pm 0.28) \times 10^{-9}$	44.1	$(1.28 \pm 0.27) \times 10^{-9}$	53.7
1.51 – 2.29	$(1.79 \pm 0.14) \times 10^{-9}$	252.9	$(1.02 \pm 0.16) \times 10^{-9}$	86.7	$(7.68 \pm 1.51) \times 10^{-10}$	50.5
2.29 – 3.47	$(1.28 \pm 0.10) \times 10^{-9}$	290.8	$(9.82 \pm 1.06) \times 10^{-10}$	189.1	$(2.91 \pm 0.90) \times 10^{-10}$	16.2
3.47 – 5.25	$(9.38 \pm 0.77) \times 10^{-10}$	323.3	$(6.14 \pm 0.73) \times 10^{-10}$	157.4	$(3.03 \pm 0.61) \times 10^{-10}$	43.4
5.25 – 7.94	$(6.54 \pm 0.60) \times 10^{-10}$	293.6	$(3.56 \pm 0.52) \times 10^{-10}$	112.5	$(2.58 \pm 0.48) \times 10^{-10}$	62.1
7.94 – 12.01	$(3.70 \pm 0.43) \times 10^{-10}$	201.5	$(2.07 \pm 0.36) \times 10^{-10}$	85.2	$(1.46 \pm 0.33) \times 10^{-10}$	40.7
12.01 – 18.18	$(2.17 \pm 0.33) \times 10^{-10}$	123.3	$(1.06 \pm 0.25) \times 10^{-10}$	43.1	$(8.80 \pm 2.51) \times 10^{-11}$	29.3
18.18 – 27.51	$(1.15 \pm 0.23) \times 10^{-10}$	77.3	$(5.30 \pm 1.77) \times 10^{-11}$	23.5	$(5.70 \pm 1.87) \times 10^{-11}$	23.6
27.51 – 41.63	$(6.20 \pm 1.70) \times 10^{-11}$	44.9	$(3.26 \pm 1.42) \times 10^{-11}$	14.1	$(2.93 \pm 1.34) \times 10^{-11}$	12.3
41.63 – 63.00	$(4.98 \pm 1.44) \times 10^{-11}$	44.7	$(3.09 \pm 1.35) \times 10^{-11}$	16.3	$(1.49 \pm 1.05) \times 10^{-11}$	5.0
63.00 – 95.33	$(1.86 \pm 0.87) \times 10^{-11}$	15.3	1.55×10^{-11}	< 5.0	$(1.64 \pm 0.90) \times 10^{-11}$	13.9
95.33 – 144.27	1.05×10^{-11}	< 5.0	1.26×10^{-11}	< 5.0	5.10×10^{-12}	< 5.0
144.27 – 218.32	1.61×10^{-11}	< 5.0	1.46×10^{-11}	< 5.0	5.27×10^{-12}	< 5.0
218.32 – 330.39	4.86×10^{-12}	< 5.0	4.86×10^{-12}	< 5.0	4.86×10^{-12}	< 5.0
330.39 – 500.00	8.82×10^{-12}	< 5.0	6.54×10^{-12}	< 5.0	5.44×10^{-12}	< 5.0

Note. — For energy bins with TS values smaller than 5.0, the upper limits at 95% confidence level are calculated.

systems exhibit a spectral break in the 1-20 GeV band and they are typically brighter in the GeV band than in the TeV band (Funk 2015; Guo et al. 2017), which is similar to Puppis A. Therefore, the γ -ray radiation mechanism of Puppis A should be very similar to that of the SNR/MC systems. Compared with the other SNR/MC systems, the lower luminosity of Puppis A in the GeV band suggests that the gas density in Puppis A may not be as high as the others (Hewitt et al. 2012). The spatial variation of the GeV spectrum shows that the broken power-law spectrum of the overall emission may have a more complicated origin due to superposition of emission from different regions with different spectra. Nevertheless, these results suggest that the spectral break decreases with the decrease of shock speed as indicated by the east-west asymmetry of the remnant in agreement with the model proposed by Ohira & Yamazaki (2016) and the general trend of spectral evolution discovered by Zeng et al. (2017).

The γ -ray emission can be produced via three radiation mechanisms: Inverse Compton Scattering (ICS) or bremsstrahlung process of high energy electrons, and the π^0 decay due to inelastic pp collisions with the latter two processes proportional to density of the background plasma. The spatial correlation between the GeV γ -ray emission and the potential clouds traced by thermal X-ray emission makes the hadron-dominated model more preferable (Katz & Waxman 2008). In addition, the theoretical explanation of GeV break also favors the hadronic scenario (Aharonian & Atoyan 1996; Gabici et al. 2009; Ohira et al. 2011; Li & Chen 2010, 2012; Uchiyama et al. 2010; Malkov et al. 2011).

3.2. Spectral Energy Distribution

In the radio band of Puppis A, Hewitt et al. (2012) reported a hint of a radio break or cutoff at ~ 40 GHz using the *WMAP* data and such spectral structure was also detected by *Planck* satellite (Arnaud et al. 2016). The X-ray emission of Puppis A is completely thermal in origin and no non-thermal component was detected. However, considering the fact that some SNRs as young as Puppis A, like RCW 86, still exist non-thermal X-ray emission (Lemoine-Goumard et al. 2012), the non-thermal component of Puppis A should not be much lower than the thermal component. Therefore, the radio structure at ~ 40 GHz is more like a break rather than a cutoff. Here, we discuss different radiation models in light of the

multi-wavelength data, including the spectral structures of the radio and GeV break.

Considering the radio break, the spectra of electrons is assumed to be a smoothly broken power law with an exponential cutoff (SBPL) in the form of

$$\frac{dN_e}{dE} \propto E^{-\alpha_e} \left(1 + \left(\frac{E}{E_{e,br}} \right)^2 \right)^{-\Delta\alpha_e/2} \exp\left(-\frac{E}{E_{e,cut}}\right). \quad (1)$$

And the spectra of protons is adopted to be a power law with an exponential cutoff (PL):

$$\frac{dN_p}{dE} \propto E^{-\alpha_p} \exp\left(-\frac{E}{E_{p,cut}}\right). \quad (2)$$

where α_i and $E_{i,cut}$ are the spectral index and the cutoff energy of particles, respectively, for $i = e$ or p . $E_{e,br}$ is the break energy and $\Delta\alpha_e$ is the spectral variation of electrons.

In the modeling, we set the spectral index of protons α_p being equal to the index of electrons below the break energy α_e , assuming that this part of the spectra are determined by the acceleration process. In addition, we assume $\Delta\alpha_e = 1$ considering the energy-loss mechanism of electrons. The distance of Puppis A is adopted to be 2.2 kpc (Reynoso et al. 2003), and the radius is $r \approx 17.6$ pc for an angular size of $55'$ at such a distance. Besides the cosmic microwave background (CMB), two IR radiation fields are taken into account ($T_1 = 150$ K, $u_1 = 0.48$ eV cm⁻³ and $T_2 = 45$ K, $u_2 = 0.2$ eV cm⁻³), which are determined by the dust emission of Puppis A (Arendt et al. 1991; Hewitt et al. 2012). The gas density, n_{gas} , ranges from 0.5 cm⁻³ to 4.0 cm⁻³, which corresponds the variation of X-ray brightness from the northeast to southwest region of Puppis A (Arendt et al. 2010; Hewitt et al. 2012). Arendt et al. (1991) and Arendt et al. (2010) gave the dust mass of 0.25 M_\odot for Puppis A by infrared observations, and considering a typical dust-to-gas ratio of 0.0077 for ISM, the gas mass of 33 M_\odot is derived (Arendt et al. 1991). However, the dust-to-gas ratio for the post-shock region of Puppis A is much lower than that for ISM and the gas mass should be much larger (Arendt et al. 2010). Nevertheless, the value of the gas mass derived from this method should be the lower limit. Meanwhile, the total mass of the gas calculated by $M_{gas} = \frac{4}{3} \pi r^3 n_{gas} m_p = 2.26 \times 10^3 (n/4.0 \text{ cm}^{-3}) M_\odot$, should be con-

sidered as an upper limit for the inhomogeneity of the actual gas density.

3.3. ICS-dominated model

The multi-wavelength spectrum energy distribution (SED) with the ICS-dominated model is shown in the top panel of Fig. 4 and the model parameters are compiled in Table 4. For the ICS-dominated model, the spectral index of electrons is 1.8. The break and cutoff energies of electrons are 20 GeV and 0.8 TeV, respectively. And the total energy of electrons above 1 GeV is estimated to be $W_e \approx 1.7 \times 10^{49}$ erg. A magnetic field strength of about $6.0 \mu\text{G}$ is needed to explain the flux in the radio band. Here the gas density, n_{gas} , is adopted to be 0.5 cm^{-3} to reduce the contribution from bremsstrahlung emission. The total energy of protons above 1 GeV, W_p , is constrained to be less than $\sim 5.0 \times 10^{49} (n/0.5 \text{ cm}^{-3})^{-1}$ erg, considering the upper-limits at several hundreds of GeV. Here, the cutoff energy of protons, $E_{p,\text{cut}}$, is adopted to be 10 TeV.

This model gives a reasonable fit to the overall spectrum. However, the inferred magnetic field, $\sim 6 \mu\text{G}$, is relatively low compared with that derived from an equipartition assumption (Dubner et al. 2013). In addition, the energy content of energetic electrons is too high if SNRs indeed dominate the cosmic ray fluxes observed at earth.

3.4. Bremsstrahlung-dominated model

To explain the emission from the radio to γ -ray band with the bremsstrahlung-dominated model, we assume a gas density of 4.0 cm^{-3} . It is interesting to note that a broken power-law electron distribution with an index of 1.85, a break energy of 18 GeV and a cutoff energy of 4.0 TeV can reproduce the spectral breaks in both the radio and γ -ray band. The corresponding magnetic field is $11.0 \mu\text{G}$ and the total energy of electrons above 1 GeV is 7.0×10^{48} erg. Here the total energy of protons above 1 GeV should be less than $\sim 3.5 \times 10^{48} (n/4.0 \text{ cm}^{-3})^{-1}$ erg for a typical cutoff energy of 10 TeV for protons to avoid overestimation of the VHE γ -ray emission. The modelled SED is shown in the middle-upper panel of Fig. 4 and the model parameters can be seen in Table 4. The spectral fit is also reasonable and the model parameters are well constrained. However, this model implies a lower energy content in energetic protons than that in electrons, which is not consistent with the supernova origin of Galactic cosmic rays.

The above lepton-dominated models can marginally explain the γ -ray emission and the radio break, considering the statistic errors of the GeV data. However, for these two models, the estimated electron to proton ratio must be much larger than 0.01, which is measured at the Earth. And these results are in agreement with the result of Hewitt et al. (2012).

3.5. Hadron-dominated model

The middle-lower panel of Fig. 4 shows the results of the hadron-dominated model fitting using the spectra of a power law with an exponential cutoff for protons and the model parameters are given in Table 4. In the modeling, the ratio of the number of relativistic electrons to protons at 1 GeV, K_{ep} , is assumed to be 0.01, which is in accord with the local measured CR abundant. The spectral indices of particles are found to be about 1.9. For electrons, a break energy of about 6 GeV,

a magnetic field strength of about $72 \mu\text{G}$ and a total energy above 1 GeV of $W_e \approx 3.2 \times 10^{47}$ erg are needed to explain the radio spectrum. The cutoff energy of electrons, $E_{e,\text{cut}} \approx 6.9$ TeV, is determined by making the acceleration timescale of diffusive shock with Borm diffusion equal to the synchrotron radiation loss timescale (Parizot et al. 2006; Funk 2015),

$$E_{e,\text{cut}} = 83.7 \left(\frac{v_{sh}}{10^3 \text{ km s}^{-1}} \right) \left(\frac{B}{1 \mu\text{G}} \right)^{-1/2} \text{ TeV} \quad (3)$$

The electron synchrotron energy loss time at the break energy 6 GeV is about 4×10^5 years which is about 2 orders of magnitude longer than the age of the remnant (4450 year, Becker et al. 2012; Winkler et al. 1988) and the shock velocity of $v_{sh} = 700 \text{ km s}^{-1}$ is used (Katsuda et al. 2013). The total energy of relativistic protons above 1 GeV is $W_p \approx 7.5 \times 10^{49} (n/4.0 \text{ cm}^{-3})^{-1}$ erg, which is very close to 10% of the typical kinetic energy released by a core-collapse supernova of $E_k \sim 10^{51}$ erg. The cutoff energy of protons is about 0.6 TeV, which is close to the result of Hewitt et al. (2012), but lower than that of electrons.

In addition to the spectra of a power law with an exponential cutoff for protons, we considered a more complex model: a smoothly broken power law with an exponential cutoff, whose form is the same as given by Equation 1 and the fitted multi-wavelength SED is compiled in the bottom panel of Fig. 4. The break energy of protons, $E_{p,\text{br}}$, is fitted to be 0.2 TeV to explain the GeV break of SED. And the cutoff energy of protons, $E_{p,\text{cut}}$, should be larger than that of the electrons, $E_{e,\text{cut}} \approx 6.9$ TeV. Other parameters listed in Table 4 are the same as that of the power law distribution for protons.

The SBPL model is very similar to the PL model except for a slightly lower TeV fluxes of the PL model with the exponential cutoff of the proton distribution. However the higher cutoff energy of the proton distribution is more reasonable and future TeV observations with better sensitivity will be able to distinguish these two models.

The hadron-dominated model can naturally explain the radio and GeV spectral break. Meanwhile, this model expects a not-too-low non-thermal X-ray emission, which is more reasonable for Puppis A compared with other young SNRs. Together with the morphology of γ -ray emission, the hadron-dominated model is the most suitable scenario to explain the multi-wavelength data of Puppis A.

The above models for the SED show that γ -ray emission from Puppis A cannot be due to interactions of background CRs with interstellar gas. In the region of Puppis A the spectral index of CRs inferred from the Galactic diffuse γ -ray emission is about 2.7 (Acero et al. 2016; Yang et al. 2016), which is close to the locally observed one but much softer than that inferred for Puppis A (see Table 4). Furthermore, the mean energy density of CRs responsible for the γ -ray emission of Puppis A, ε_p , derived with $n_{\text{gas}} \times W_p / (\frac{M_{\text{gas}}}{m_p})$, is higher than that of the background CRs. Therefore, the γ -ray emission is most likely produced by particles accelerated by shocks of the SNR Puppis A.

4. CONCLUSION

In this work, we re-analyze the γ -ray emission from SNR Puppis A using seven years Fermi-LAT data with the latest Pass 8 version. The γ -ray morphology of Puppis A is well correlated with its thermal X-ray and IR emissions rather than the radio emission. This means that some dense clouds may

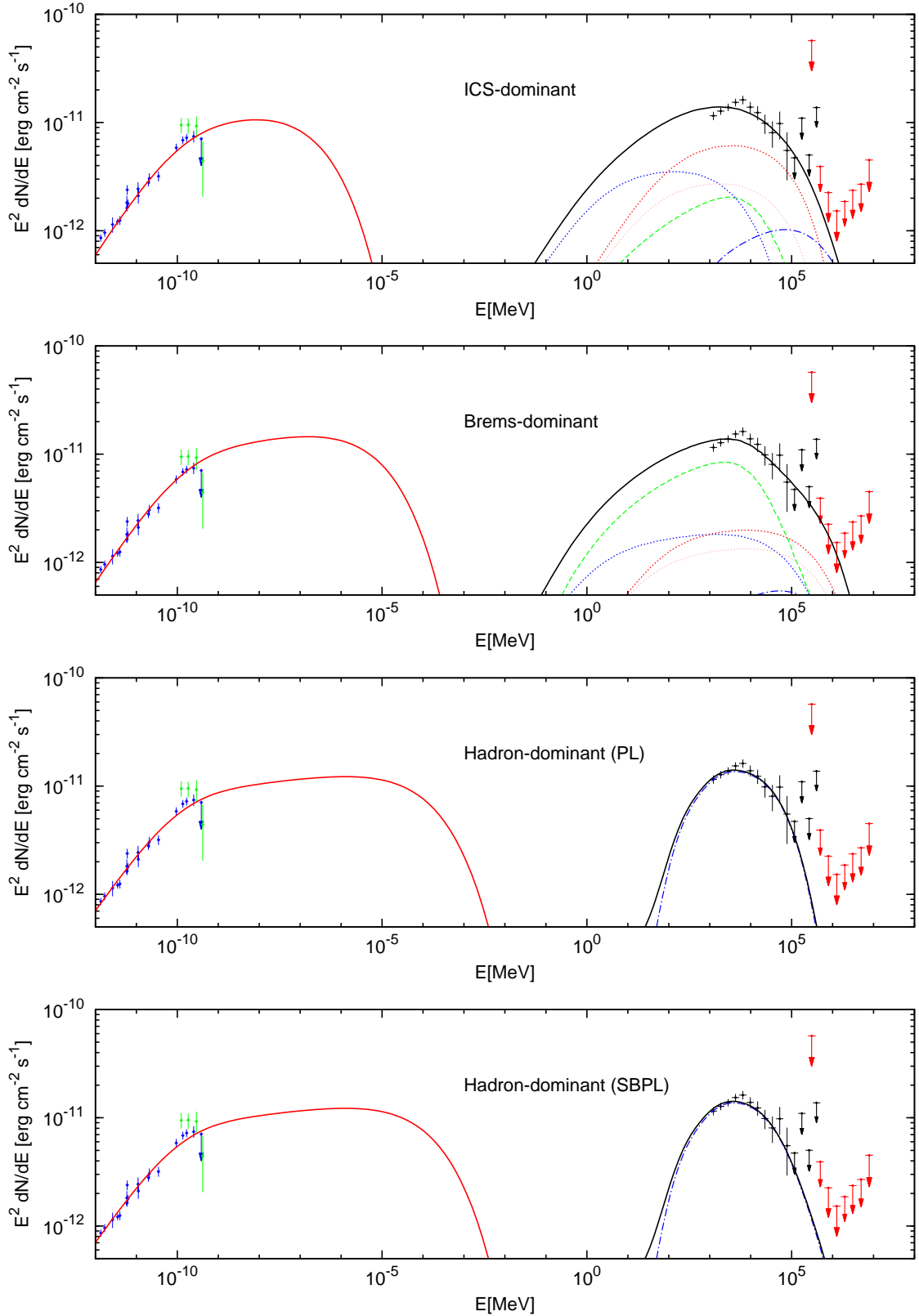


FIG. 4.— Different emission models fitting on the multi-wavelength data of Puppis A with the parameters listed in Table 4. The hadron-dominated models with the spectra of a power law and a smoothly broken power law for protons are plotted separately. In each panel, the radio data marked by blue and green points are observed by *WMAP* (Hewitt et al. 2012) and *Planck* satellites (Arnaud et al. 2016), respectively. And the radio emission is dominated by the synchrotron component, shown as the red solid curve. For the γ -ray emission, the contributions from ICS, bremsstrahlung, and π^0 -decay processes are shown as the dotted, dashed and dotted-dashed lines, respectively. The ICS emission includes three components from CMB (blue) and two infrared (red and pink) photon fields. The black solid line represents the sum of different radiation components.

TABLE 4
PARAMETERS FOR THE MODELS

Model	α_p	α_e	$\Delta\alpha_e$	$E_{p,br}$ (TeV)	$E_{p,cut}$ (TeV)	$E_{e,br}$ (GeV)	$E_{e,cut}$ (TeV)	B (μG)	W_e^a (10^{49}erg)	$n_{\text{gas}} \times W_p^{a,b}$ ($10^{49}\text{erg cm}^{-3}$)	ε_p^c ($eV \text{ cm}^{-3}$)
ICS-dominated	1.80	1.80	1.0	–	10.0	20.0	0.8	6.0	1.7	2.5	46.5
Brems-dominated	1.85	1.85	1.0	–	4.0	18.0	4.0	11.0	0.7	1.4	3.3
Hadron-dominated (PL)	1.90	1.90	1.0	–	0.6	6.0	6.9	72.0	3.2×10^{-2}	30.0	69.8
Hadron-dominated (SBPL)	1.90	1.90	1.0	0.2	> 6.9	6.0	6.9	72.0	3.2×10^{-2}	30.0	69.8

NOTE. —

a) The total energy of relativistic particles, $W_{e,p}$, is calculated for $E > 1$ GeV.

b) For the ICS-dominated model, the gas density, $n_{\text{gas}} = 0.5$ is adopted; for the Brems- and Hadron-dominated models, $n_{\text{gas}} = 4.0$ is adopted.

c) The energy density of CRs, ε_p , is calculated by $n_{\text{gas}} \times W_p = \frac{M_{\text{gas}}}{m_p} \varepsilon_p$. Here the total mass of the gas, M_{gas} is defined as $M_{\text{gas}} = \frac{4}{3} \pi r^3 n_{\text{gas}} m_p$, assuming a homogeneous gas density for the whole volume of Puppis A.

exist around Puppis A for providing the target particles of the high energy γ -ray emission. The γ -ray spectra of Puppis A exhibits a break at 7.92 ± 1.91 GeV with a significance of $\sim 5.6\sigma$. And the photon indices below and above the break energy are 1.81 ± 0.08 and 2.53 ± 0.12 , respectively. The existence of the GeV break can naturally explain the upper limit derived from HESS observations in the TeV band.

We use three radiation mechanisms, including the ICS-, bremsstrahlung- and hadron-dominated models, to fit the multi-wavelength data. Although the ICS- and bremsstrahlung-dominated models can marginally explain the γ -ray emission, the hadron-dominated model seems to be more plausible considering the spectral structure of the GeV break and the radio break detected by *WMAP* and *Planck* satellites. However, the decisive evidence of the hadron-

dominated model may rely on the detection of the characteristic “ π^0 bump” in the lower energy band. Meanwhile, the hadron-dominated model also predicts a not-too-low non-thermal X-ray emission of Puppis A, which may be confirmed by the future X-ray observations.

ACKNOWLEDGMENTS

This work was supported in part by National Key Program for Research and Development (2016YFA0400200), 973 Programme of China under grants 2013CB837000 and 2014CB845800, the 100 Talents program of Chinese Academy of Sciences, National Natural Science of China under grants 11433009 and 11233001, the Strategic Priority Research Program, the Emergence of Cosmological Structures, of the Chinese Academy of Sciences, Grant No. XDB09000000.

REFERENCES

- Abdo, A. A., Ackermann, M., Ajello, M., et al. 2009, *ApJL*, 706, L1
 Abdo, A. A., Ackermann, M., Ajello, M., et al. 2010a, *ApJ*, 712, 459
 Abdo, A. A., Ackermann, M., Ajello, M., et al. 2010b, *Sci*, 327, 1103
 Abdo, A. A., Ackermann, M., Ajello, M., et al. 2010c, *ApJ*, 718, 348
 Abdo, A. A., Ackermann, M., Ajello, M., et al. 2010d, *ApJ*, 722, 1303
 Abramowski, A., Aharonian, F., Ait Benkhali, F., et al. 2015, *A&A*, 575, 81
 Acero, F., Ackermann, M., Ajello, M., et al. 2015, *ApJ*, 218, 23
 Acero, F., Ackermann, M., Ajello, M., et al. 2016, *ApJS*, 223, 26
 Ackermann, M., Ajello, M., Allafort, A., et al. 2013, *Sci*, 339, 807
 Aharonian, F., & Atoyan, A. M., 1996, *A&A*, 309, 917
 Ajello, M., Allafort, A., Baldini, L., et al. 2012, *ApJ*, 744, 80
 Arendt, R. G., Dwek, E., & Petre, R. 1991, *ApJ*, 368, 474
 Arendt, R. G., Dwek, E., Blair, W. P., et al. 2010, *ApJ*, 725, 585
 Arnaud, M., Ashdown, M., Atrio-Barandela, F., et al. (Planck Collaboration) 2016, *A&A*, 586, A134
 Achterberg, A., Blandford, R. D., & Reynolds, S. P. 1994, *A&A*, 281, 220
 Becker, W., Prinz, T., Winkler, P. F., & Petre, R. 2012, *ApJ*, 755, 141
 Dubner, G., Loiseau, N., Rodriguez-Pascual, P., et al. 2013, *A&A*, 555, A9
 Dwek, E., Petre, R., Szymkowiak, A., & Rice, W. L. 1987, *ApJL*, 320, L27
 Funk, S. 2015, *Annual Review of Nuclear and Particle Science*, 65, 245
 Gabici, S., Aharonian, F., & Casanova, S., 2009, *MNRAS*, 396, 1629
 Giuliani, A., Cardillo, M., Tavani, M., et al. 2011, *ApJL*, 742, L30
 Grenier, I. A., Casandjian, J.-M., & Terrier, R. 2005, *Science*, 307, 1292
 Guo, X.-L., Xin, Y.-L., Liao, N.-H., et al. 2017, *ApJ*, 835, 42
 Hanabata, Y., Katagiri, H., Hewitt, J. W., et al. 2014, *ApJ*, 786, 145
 Hewitt, J. W., Grondin, M.-H., Lemoine-Goumard, M., et al. 2012, *ApJ*, 759, 89
 Hillas A. M., 2005, *J. Phys. G: Nucl. Part. Phys.*, 31, R95
 Hui, C. Y., & Becker, W. 2006b, *A&A*, 454, 543
 Humensky, B., & for the VERITAS Collaboration 2015, arXiv:1512.01911
 Hwang, U., Flanagan, K. A., & Petre, R., 2005, *ApJ*, 635, 355
 Hwang, U., Petre, R., & Flanagan, K. A., 2008, *ApJ*, 676, 378
 Jogler, T., & Funk, S. 2016, *ApJ*, 816, 100
 Katagiri, H., Tibaldo, L., Ballet, J., et al. 2011, *ApJ*, 741, 44
 Katsuda, S., Mori, K., Tsunemi, H., et al. 2008, *ApJ*, 678, 297
 Katsuda, S., Hwang, U., Petre, R., et al. 2010, *ApJ*, 714, 1725
 Katsuda, S., Tsunemi, H., Mori, K., et al. 2012, *ApJ*, 756, 49
 Katsuda, S., Ohira, Y., Mori, K., et al. 2013, *ApJ*, 768, 182
 Katz, B., & Waxman, E. 2008, *JCAP*, 1, 018
 Lee, S.-H., Patnaude, D. J., Raymond, J. C., et al. 2015, *ApJ*, 806, 71
 Lemoine-Goumard, M., Renaud, M., Vink, J., et al. 2012, *A&A*, 545, A28
 Li, H., & Chen, Y., 2010, *MNRAS*, 409, L35
 Li, H., & Chen, Y., 2012, *MNRAS*, 421, 935
 Liu, B., Chen, Y., Zhang, X., et al. 2015, *ApJ*, 809, 102
 Malkov, M. A., Diamond, P. H., & Sagdeev, R. Z., 2011, *Nature Communications*, 2, 194
 Mauch, T., Murphy, T., Buttery, H. J., et al. 2003, *MNRAS*, 342, 1117
 Miville-Deschênes, M.-A., & Lagache, G. 2005, *ApJS*, 157, 302
 Ohira, Y., Murase, K., & Yamazaki, R., 2011, *MNRAS*, 410, 1577
 Ohira, Y., & Yamazaki, R. 2016, arXiv:1609.02266
 Parizot, E., Marcowith, A., Ballet, J., & Gallant, Y. A., 2006, *A&A*, 453, 387
 Paron, S., Dubner, G., Reynoso, E., & Rubio, M. 2008, *A&A*, 480, 439
 Petre, R., Canizares, C. R., Kriss, G. A., Winkler, P. F., 1982, *ApJ*, 258, 22
 Petre, R., Becker, C. M., Winkler, P. F., 1996, *ApJ*, 465, L43
 Reynoso, E. M., Green, A. J., Johnston, S., et al. 2003, *MNRAS*, 345, 671
 Tatischeff, V., Tavani, M., von Ballmoos, P., et al. 2016, *Proc. SPIE*, 9905, 99052N
 Uchiyama, Y., Blandford, R. D., Funk, S., et al. 2010, *ApJL*, 723, L122
 Winkler, P. F., Tuttle, J. H., Kirshner, R. P., & Irwin, M. J. 1988, in *IAU Colloq. 101: Supernova Remnants and the Interstellar Medium*, ed. R. S. Roger & T. L. Landecker (Cambridge: Cambridge Univ. Press), 65
 Xing, Y., Wang, Z., Zhang, X., & Chen, Y. 2015, *ApJ*, 805, 19
 Yang, R., Aharonian, F., & Evoli, C. 2016, *PRD*, 93, 123007
 Zavlin, V. E., Trümper, J., Pavlov, G. G., 1999, *ApJ*, 525, 959
 Zeng, H., Xin, Y., Liu, S., et al. 2017, *ApJ*, 834, 153
 Zhang, X., Chen, Y., Li, H., & Zhou, X. 2013, *MNRAS*, 429, L25